

2MASS wide field extinction maps: II. The Ophiuchus and the Lupus cloud complexes

Marco Lombardi^{1,2}, Charles J. Lada³, and João Alves⁴

¹ European Southern Observatory, Karl-Schwarzschild-Straße 2, D-85748 Garching bei München, Germany

² University of Milan, Department of Physics, via Celoria 16, I-20133 Milan, Italy (on leave)

³ Harvard-Smithsonian Center for Astrophysics, Mail Stop 42, 60 Garden Street, Cambridge, MA 02138

⁴ Calar Alto Observatory – Centro Astronómico Hispano Alemán, C/Jesús Durbán Remón 2-2, 04004 Almería, Spain

Received ***date***; Accepted ***date***

ABSTRACT

We present an extinction map of a ~ 1700 deg sq region that encloses the Ophiuchus, the Lupus, and the Pipe dark complexes using 42 million stars from the Two Micron All Sky Survey (2MASS) point source catalog. The use of a robust and optimal near-infrared method to map dust column density (NICER, described in Lombardi & Alves 2001) allow us to detect extinction as low as $A_K = 0.05$ mag with a $2\text{-}\sigma$ significance, and still to have a resolution of 3 arcmin on our map. We also present a novel, statistically sound method to characterize the small-scale inhomogeneities in molecular clouds. Finally, we investigate the cloud structure function, and show that significant deviations from the results predicted by turbulent models are observed.

Key words. ISM: clouds, dust, extinction, ISM: structure, ISM: individual objects: Pipe molecular complex, Methods: data analysis

1. Introduction

In this paper we present an extinction map of the Ophiuchus and Lupus complexes covering ~ 1700 deg sq, computed by applying an optimized multi-band technique dubbed Near-Infrared Color Excess Revisited (NICER Lombardi & Alves 2001, hereafter Paper I) to 42 million JHK photometric measurements of stars from the Two Micron All Sky Survey (2MASS; Kleinmann et al. 1994). This paper is the second of a series where we apply the NICER method to point sources from the 2MASS database. The main aim of this coordinated study is to investigate in detail the large-scale structure of molecular clouds. In addition, the use of a uniform dataset and of a consistent and well tested pipeline allows us to characterize many properties of molecular clouds, such as their reddening law, and to identify cloud-to-cloud variations in such properties. The region considered here encloses in addition the Pipe nebula, considered in the first paper of this series (Lombardi et al. 2006; hereafter Paper II), and allows us to study in detail the relationships among these molecular clouds.

Lupus is a well studied complex, composed of several subclouds showing different modes of star formation: Lupus 1 shows isolated star formation, while cluster formation is observed in Lupus 3 (Schwartz 1977; Hughes et al. 1994; Nakajima et al. 2000); no evident star formation activity is observed in Lupus 5. The distance of this cloud complex is still highly controversial. The conventional value, 150 pc (Krautter 1991), has been challenged by Knude & Hog (1998), who reported 100 pc, and by Wichmann et al. (1998), 190 pc, both using Hipparcos observations. In ad-

dition, Knude & Nielsen (2001) suggested that Lupus 2 is physically disconnected from the other Lupus subclouds, and is located at a distance of 360 pc; similarly, Bertout et al. (1999) suggested Lupus 3 to be disconnected from the rest of the Lupus complex. However, surprisingly no velocity difference is found among the various Lupus subclouds in radio observations. Recently, we used a novel maximum-likelihood technique based on Hipparcos data obtaining $d = (155 \pm 8)$ pc (Lombardi et al. 2008); this value will be adopted in this paper as the actual distance of Lupus.

Due to its large area on the sky, millimeter observations have mostly covered limited regions of this cloud. The first extensive cloud survey in ^{12}CO ($J = 1 \rightarrow 0$) was made by Murphy et al. (1986) over ~ 170 sq deg with an effective resolution of 30 arcmin. More recently, Tachihara et al. (2001) have performed a complete survey of the Lupus complex (also in ^{12}CO , $J = 1 \rightarrow 0$) using the NANTEN sub-millimeter telescope. Their data covered 550 sq deg on a grid of 8 arcmin, and smaller areas on a 4 arcmin grid. Finally, recently Teixeira et al. (2005) studied the structure of Lupus 3 in the NIR.

The ρ Ophiuchi molecular cloud is a filamentary complex located at the edge of the Upper Scorpius subgroup in the Sco-Cen OB association. It is composed of a series of dark clouds that extend eastward from cores of dense molecular gas (de Geus 1992). With an estimated distance of (119 ± 6) pc (Lombardi et al. 2008), it is one of the nearest star-forming regions, and has thus been the target of numerous investigations. The main cloud, L1688, is situated about one degree south of the star ρ Ophiuchi and has been studied in the near and far infrared, in the millimeter continuum, as well as in the X-ray and radio continuum, and hosts an embedded infrared cluster with ~ 200 young stel-

lar objects (YSO; e.g., Greene & Young 1992; Bontemps *et al.* 2001; Comeron *et al.* 1993; Tachihara *et al.* 2000). L1688 is known to host a $1 \text{ pc} \times 2 \text{ pc}$ central molecular core with visual estimated visual extinction exceeding 50 mag (Wilking & Lada 1983). This “main cloud” of Oph covers an area of roughly 480 sq arcmin and has been dissected into about a dozen cloud components. The entire star formation complex extends over several degrees on the sky, containing a few major clouds. Motte *et al.* (1998) have conducted an extensive 1.3 mm continuum mapping of the central region using the IRAM 30-m telescope. Stanke *et al.* (2006) presents SIMBA 1.2 mm observations of the cloud covering an area of 4600 arcmin² with a resolution of $24''$; Johnstone *et al.* (2000) have published a SCUBA 850 μm thermal emission map of the ρ Ophiuchi cloud.

This paper is organized as follows. In Sect. 2 we briefly describe the technique used to map the dust and we present the main results obtained. A statistical analysis of our results and a discussion of the bias introduced by foreground stars and unresolved substructures is presented in Sect. 3. Section 4 is devoted to the mass estimate of the cloud complex. Finally, we summarize the results obtained in this paper in Sect. 5.

2. Nicer extinction map

We carried out the data analysis using the NICER method described in Paper I. Near infrared J ($1.25 \mu\text{m}$), H ($1.65 \mu\text{m}$), and K_s band ($2.17 \mu\text{m}$) magnitudes of stars in a large region of the sky which includes the Ophiuchus and the Lupus dark clouds were taken from the Two Micron All Sky Survey¹ (2MASS; Kleinmann *et al.* 1994). In particular, we selected all 2MASS reliable point sources within the boundaries

$$-32^\circ < l < +16^\circ, \quad +2^\circ < b < +40^\circ. \quad (1)$$

This area is 1672 square degrees and contains approximately 42 million point sources from the 2MASS catalog. Note that since the region spans several degrees in galactic latitude, the local density of background stars changes significantly in the field; as a result, since we used a fixed size for the smoothing of the extinction map (see below), the noise of the map increases as b increases.

When selecting stars from the 2MASS point source catalog we discarded possible spurious detections (e.g., objects likely to be associated to solar system minor bodies, extended sources, or artifacts). We then generated a preliminary extinction map which, as described in Paper I, was mainly used as a first check of the parameters adopted, to select a control region on the field, and to obtain the photometric parameters to be used in the final map (see Fig. 6). We identified a large region that is apparently affected by only a negligible extinction (see below), and used the colors of stars in this control field as reference ones.

Using the information provided by the control field, we generated a second map, which is thus “calibrated” (i.e., provides already, for each position in our field, a reliable estimate of the column density). Note that the recent Indebetouw *et al.* (2005) 2MASS reddening law was used here. We then considered the color-color diagram for the

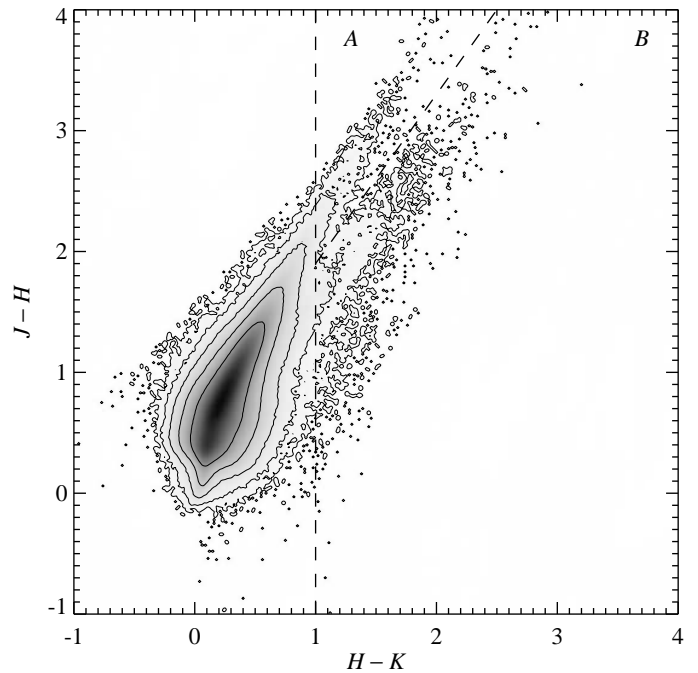


Fig. 1. Color-color diagram of the stars in the whole field, as a density plot. The contours are logarithmically spaced, i.e. each contour represents a density ten times larger than the enclosing contour; the outer contour detects single stars and clearly shows a bifurcation at large color-excesses. The dashed lines identify the regions in the color space defined in Eqs. (2) and (3), as indicated by the corresponding letters. Only stars with accurate photometry in all bands (maximum $1\text{-}\sigma$ errors allowed 0.1 mag) have been included in this plot.

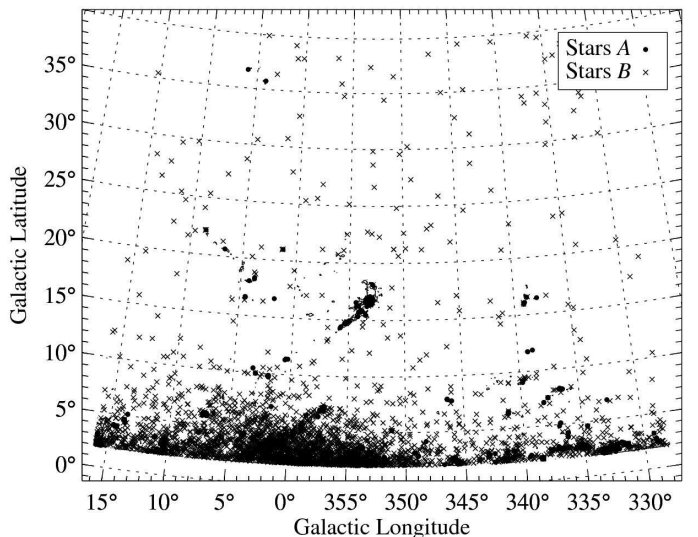


Fig. 2. Spatial distribution of the samples of sources as defined by Eqs. (2) and (3). Sample A is shown as filled circles, while sample B is shown as crosses (see also Fig. 1). Sample A appears to be strongly clustered in high-column density regions of the cloud, and is thus interpreted as genuine reddened stars; sample B seems not to be associated with the cloud, and is instead preferentially located at low galactic latitudes and in the Galactic bulge.

¹ See <http://www.ipac.caltech.edu/2mass/>.

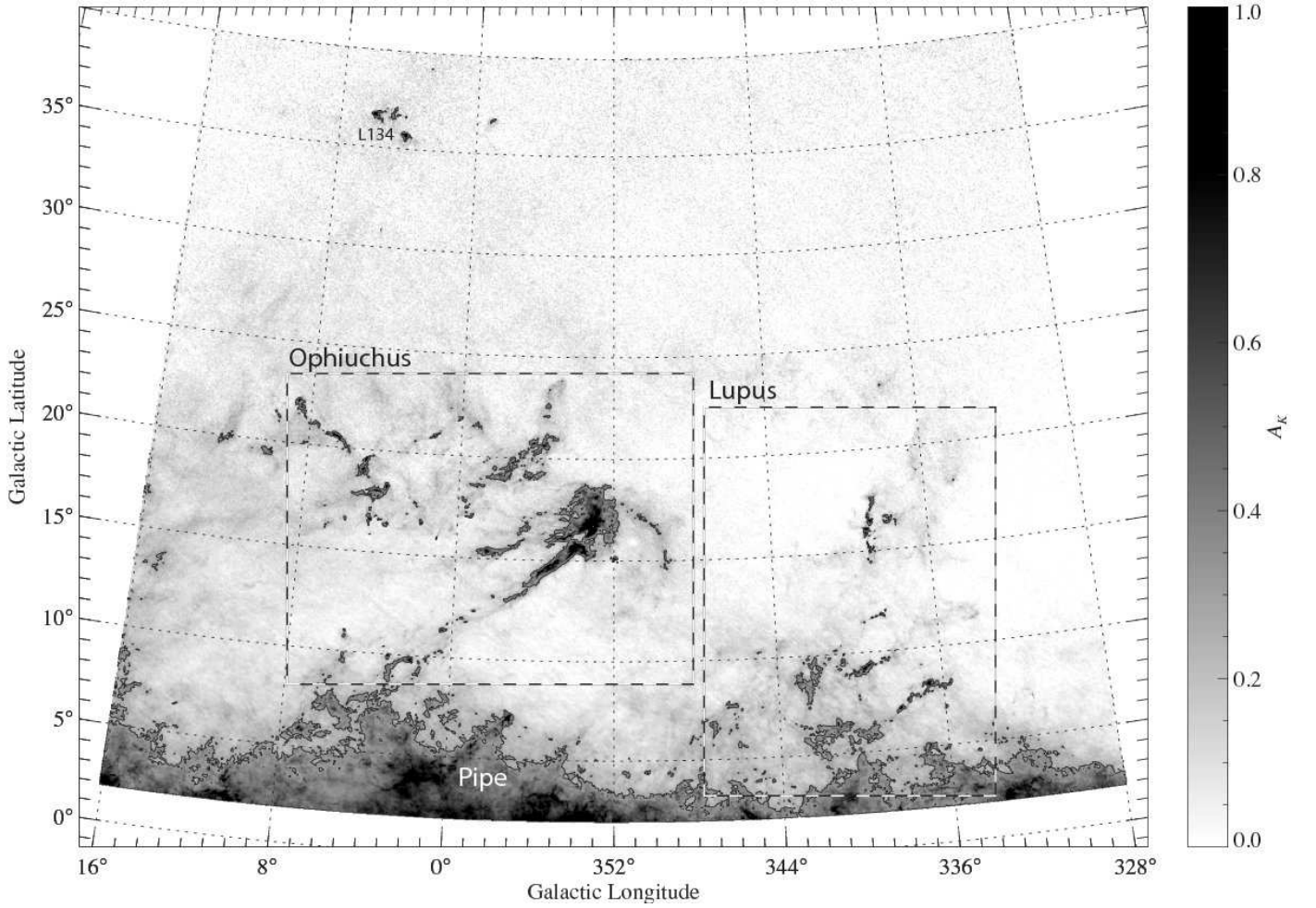


Fig. 6. The NICER extinction map of the Ophiuchus, Lupus, and Pipe complexes. The resolution is $\text{FWHM} = 3$ arcmin. The various dashed boxes mark the regions shown in greater detail in Figs. 9 and 10. The overplotted contour is at $A_K = 0.3$ mag. The Pipe nebula occupies the region around $(l, b) = (0^\circ, 5^\circ)$.

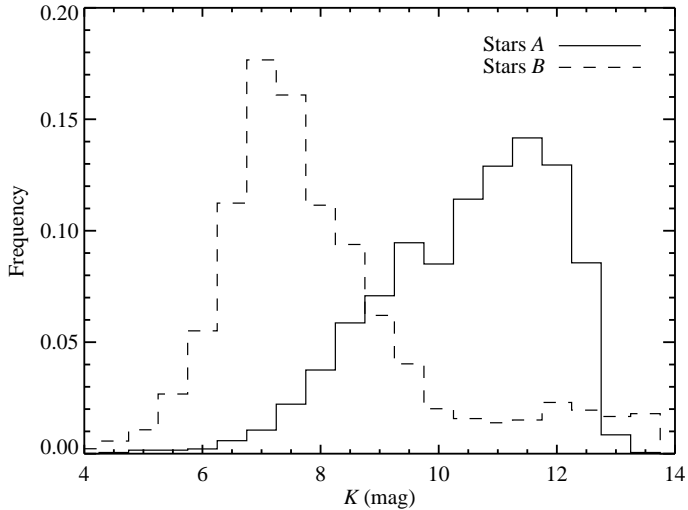


Fig. 3. The histogram of the K band magnitude for the two star subsets A and B of Eqs. (2) and (3).

lous star colors. The result, presented in Fig. 1, shows a bifurcation for $H - K > 1$ mag.

As discussed in detail in Paper II, the bifurcation is likely to be created by Asymptotic Giant Branch (AGB) stars. To further investigate this point, we considered the two samples in the color-color diagram defined as

$$A \equiv \{1.4(H - K) + 0.5 \text{ mag} < (J - H) \text{ and } H - K > 1 \text{ mag}\}, \quad (2)$$

$$B \equiv \{1.4(H - K) + 0.5 \text{ mag} > (J - H) \text{ and } H - K > 1 \text{ mag}\}. \quad (3)$$

An analysis of the spatial distribution of these two samples (Fig. 2) reveals that, as expected, sample A is associated with the densest regions of the molecular cloud, while sample B is distributed on the whole field with a strong preference for low galactic latitude regions.

The nature of the two stellar populations in samples A and B is further clarified by the histogram of their K band magnitudes, shown in Fig. 3. As expected, sample A shows a broad distribution, which can be essentially described as a simple power-law luminosity function up to $K \simeq 12$ mag; note that the completeness limit of our sample is significantly smaller than the typical 2MASS completeness in the

stars in the catalog to check for possible signs of anoma-

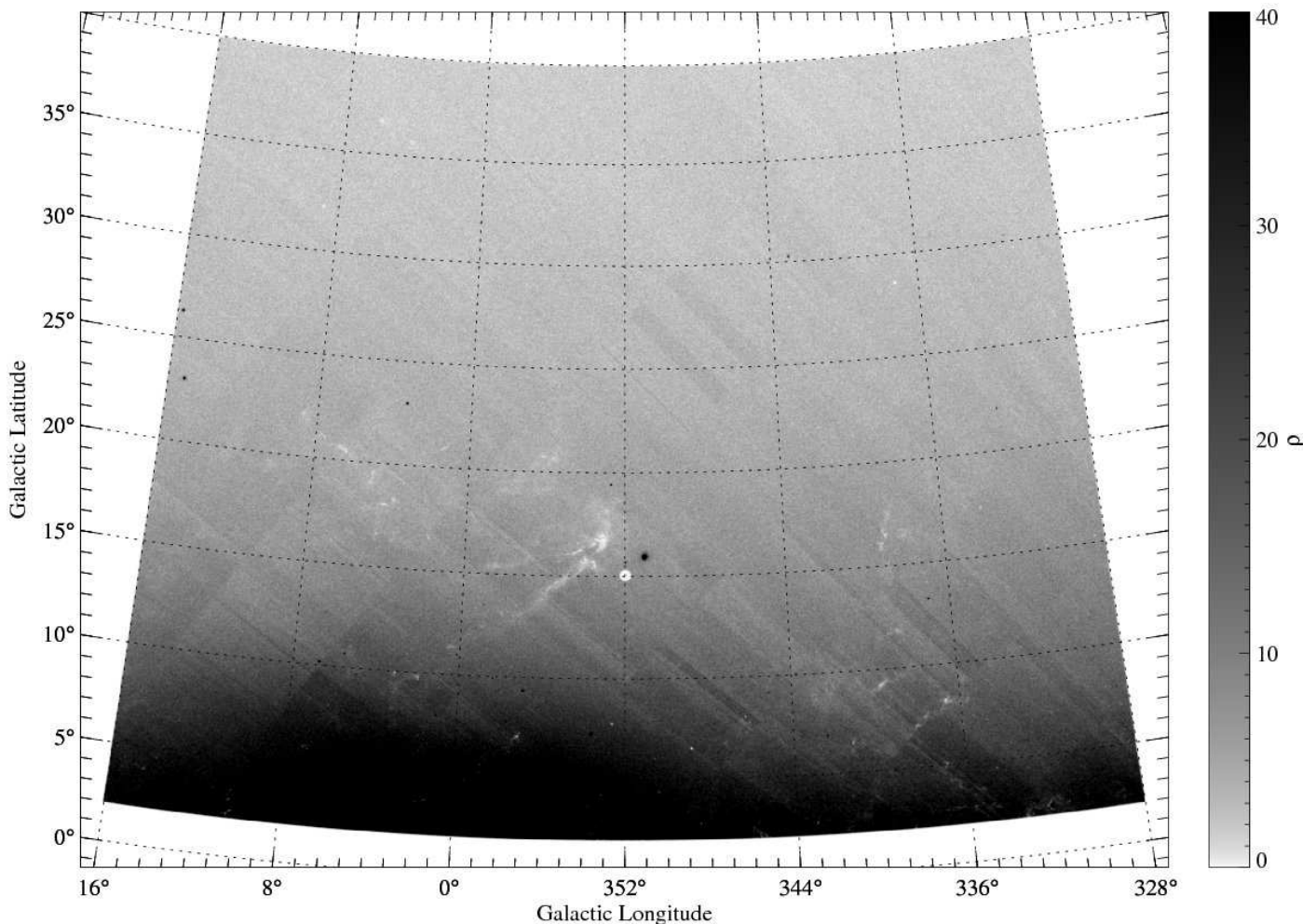


Fig. 7. The star density for the extinction map of Fig. 6; note how evident is the galactic bulge here. The faint white structures correspond to the position of dense cores, where the star density decreases because of the cloud extinction. The white “hole” at the center-bottom of the field is Antares. The black spots are open and globular clusters.

K band (14.3 mag at 99% completeness) because of the stricter selection operated here (small photometric errors in all bands) and because most sample A stars come from low galactic latitude regions (where the increased density of stars significantly reduces the completeness of the 2MASS). In contrast to sample A stars, sample B stars show a well defined distribution, with a pronounced and relatively narrow peak at $K \simeq 7$ mag. This strongly suggests that we are looking at a *homogeneous* population of sources located at essentially the same *distance*.

The lack of correlation between the dust reddening and the stars of sample B can be also investigated by considering the extinction-corrected color-color diagram shown in Fig. 4. This plot was obtained by estimating, for each star, its “intrinsic” colors, i.e. the extinction corrected colors from the extinction at the star’s location as provided by the NICER map. In other words, we computed

$$J_{\text{intr}} \equiv J - (A_J/A_K)\hat{A}_K, \quad (4)$$

$$H_{\text{intr}} \equiv H - (A_H/A_K)\hat{A}_K, \quad (5)$$

$$K_{\text{intr}} \equiv K - \hat{A}_K, \quad (6)$$

where \hat{A}_K is the NICER estimated extinction in the direction of the star from the angularly close objects. By com-

paring Fig. 4 with Fig. 1, we see that the upper branch, i.e. sample A , is strongly depressed, while the lower branch (sample B) is largely unaffected. Note that the residual stars appearing in the upper branch are likely to be the effect of an inaccurate extinction correction due to small-scale inhomogeneities not captured by our analysis; similarly, the tail at negative colors is due to “over-corrected” stars (for example foreground stars observed in projection to a cloud). Because of the much shrunken distribution of the upper-branch, Fig. 4 is particularly useful to better identify stars belonging to the lower branch, and was thus used to define two further subsets:

$$B_1 \equiv \left\{ |(J - H)_{\text{intr}} - 1.4(H - K)_{\text{intr}} + 0.5| < 0.9 \right. \\ \left. \text{and } (J - H)_{\text{intr}} > -4.6(H - K)_{\text{intr}} + 4 \right\}. \quad (7)$$

$$B_2 \equiv \left\{ |(J - H)_{\text{intr}} - 1.4(H - K)_{\text{intr}} + 0.5| < 0.9 \right. \\ \left. \text{and } (J - H)_{\text{intr}} > -2.1(H - K)_{\text{intr}} + 2.5 \right\}. \quad (8)$$

These two subsets, marked in Fig. 4, correspond to the areas in the color-color plot where a contamination by sample B stars is possible (B_1), or highly likely (B_2). We find approximately 996 000 B_1 stars and 360 000 B_2 ones, corresponding to 2.3% and to 0.88% respectively.

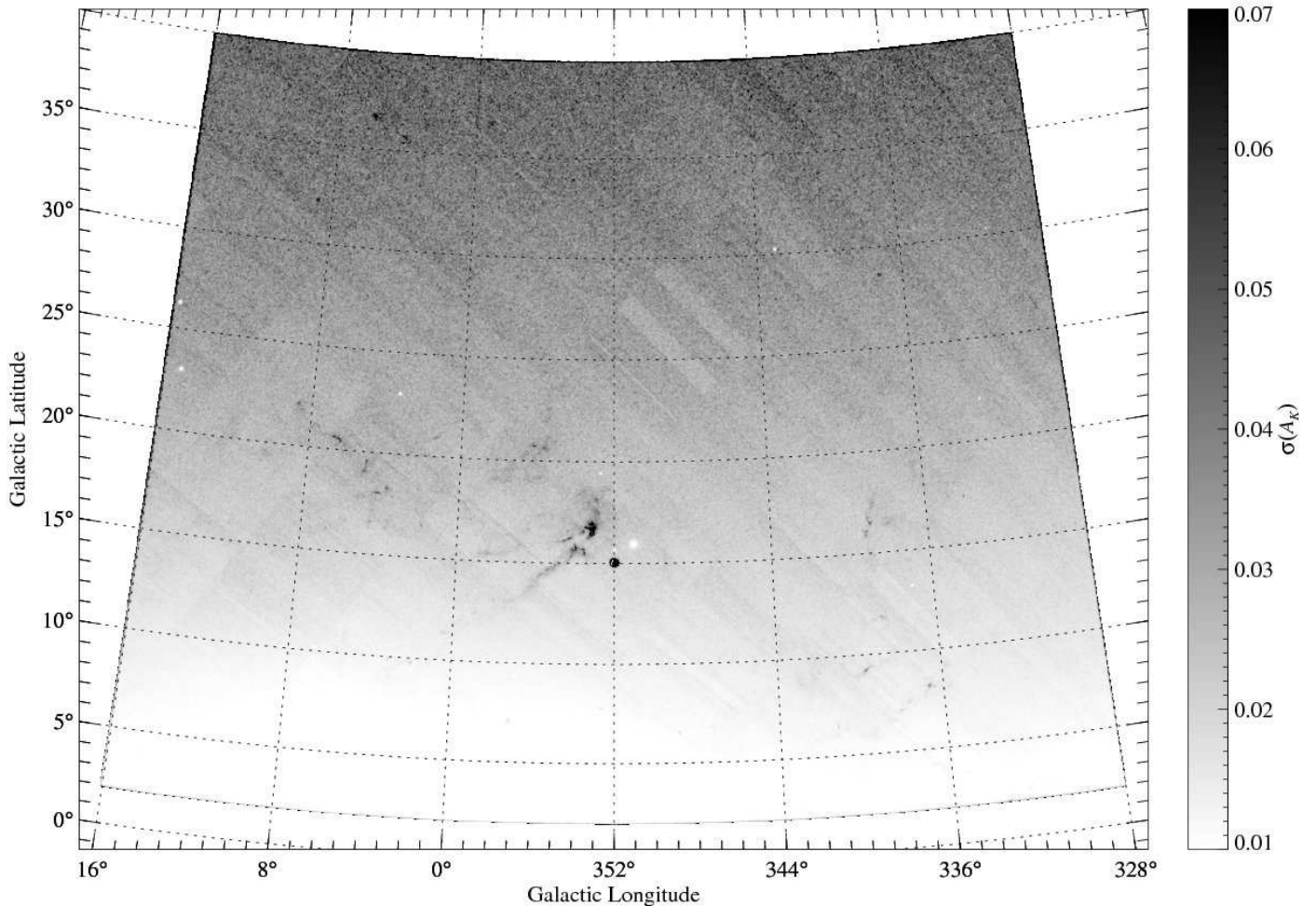


Fig. 8. The statistical error $\sigma(A_K)$ on the measured column density of Fig. 6. Note that correlation on the errors on a scale of FWHM = 3 arcmin is expected. The increase of the error with the galactic latitude is evident.

In summary, all the evidence found supports the identification of the “lower branch” with evolved intermediate mass stars (about 1 to 7 M_{\odot}), and likely with the Asymptotic Giant Branch (AGB) at about the distance to the Galactic center (see also Paper II). Since the “lower branch” stars seem to be unrelated to the molecular cloud, and since their colors would be interpreted by the NICER algorithm as a sign of extinction, in principle our results could be biased toward a higher extinction, especially at low galactic latitude regions. In practice, we argue that the bias introduced by “lower branch” stars is negligible given the low density of these stars.

Nevertheless, and in order to avoid any source of bias, although small, we excluded from the 2MASS catalogs all stars located in the B_2 color-space region, and performed the whole analysis described in this paper using this reduced subset of stars. We stress that if we had performed a cut in the *observed* colors, we would have introduced a new bias in the deduced column density; instead, a selection in the *intrinsic* colors does not bias the final results. As an example, Fig. 5 shows the color-color diagram for the new set of stars: note that the “lower branch” disappears completely in this plot, a further confirmation that our selection is effective in removing this population of stars.

We then run again the whole NICER pipeline on the refined catalog. After (re)evaluating the statistical properties of stars in the control field, we constructed the final map, shown in Fig. 6. We recall that in NICER the final map can be generated using different smoothing techniques (see Lombardi 2002 for a discussion on the characteristics and merits of various interpolators). As pointed out in Paper I, generally these techniques produce comparable results, and thus we focused here to the simple moving weight average:

$$\hat{A}_K(\boldsymbol{\theta}) = \frac{\sum_{n=1}^N W^{(n)}(\boldsymbol{\theta}) \hat{A}_K^{(n)}}{\sum_{n=1}^N W^{(n)}}, \quad (9)$$

where $\hat{A}_K(\boldsymbol{\theta})$ is the extinction at the angular position $\boldsymbol{\theta}$, $\hat{A}_K^{(n)}$ is the extinction of the n -th star, and $W^{(n)}(\boldsymbol{\theta})$ is the weight for the n -th star for the pixel at the location $\boldsymbol{\theta}$:

$$W^{(n)}(\boldsymbol{\theta}) = \frac{W(\boldsymbol{\theta} - \boldsymbol{\theta}^{(n)})}{\text{Var}(\hat{A}_K^{(n)})}. \quad (10)$$

Hence, the weight for the n -th star is composed by two factors: (i) $W(\boldsymbol{\theta} - \boldsymbol{\theta}^{(n)})$, i.e. a function of the angular distance between the star and the point $\boldsymbol{\theta}$ where the extinction has to be interpolated, and (ii) $\text{Var}(\hat{A}_K^{(n)})$, the inverse of the

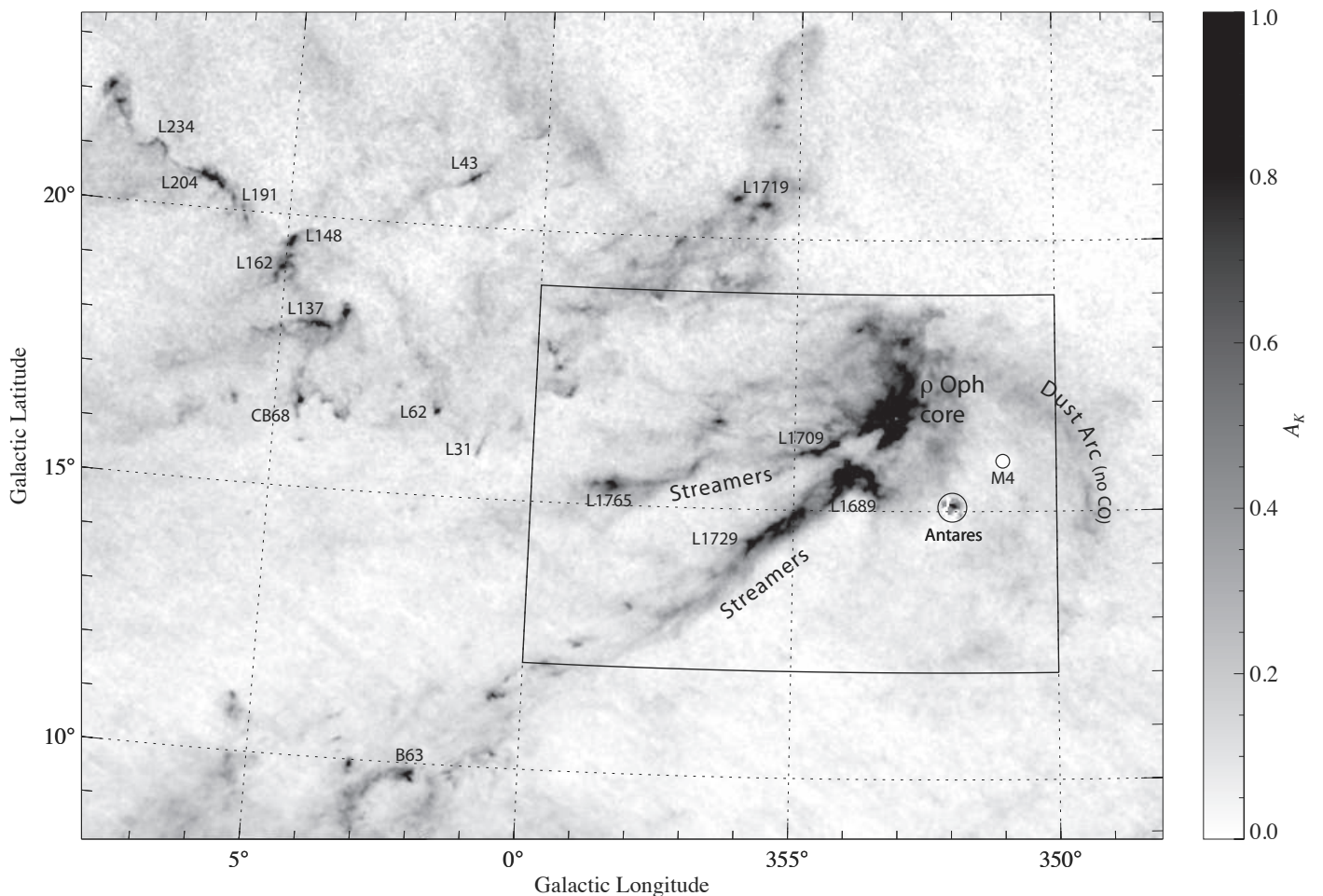


Fig. 9. A zoom of Fig. 6 showing the central region of the Ophiuchus cloud. The box encloses the core of cloud, for which a few separate studies are presented in this paper.

inferred variance on the estimate of A_K from the star. The first factor, parametrized by the weight function W , is here taken to be a Gaussian.

The map of Fig. 6 was generated on a grid of approximately 2000×1600 points, with scale 90 arcsec per pixel, and with Gaussian smoothing characterized by $\text{FWHM} = 3$ arcmin. Note that in the weighted average of Eq. (9) we also introduced an iterative σ -clipping at $3\text{-}\sigma$ error (see Paper I). The average, *effective* density of stars is ~ 6.5 stars per pixel, but as noted above this value changes significantly on the field with the galactic latitude (see Fig. 7); this density guarantees an average ($1\text{-}\sigma$) error on A_K below 0.03 magnitudes. The largest extinction was measured close to ρ Ophiuchi, where $A_K \simeq 2.89$ magnitudes. The expected error on the extinction A_K is shown in Fig. 8, and was evaluated from the relation (see Paper II)

$$\sigma_{\hat{A}_K}^2(\theta) \equiv \frac{\sum_{n=1}^N [W^{(n)}(\theta)]^2 \text{Var}(\hat{A}_K^{(n)})}{\left[\sum_{n=1}^N W^{(n)}(\theta)\right]^2}. \quad (11)$$

As expected, we observe a significant gradient along the galactic latitude. Other variations in the expected errors can be associated to bright stars (they produce the characteristic cross-shaped patterns), to globular clusters (white dots in Fig. 8), and to the cloud itself (dark areas). Because

of the relatively large variations on the noise of the extinction map, clearly a detailed analysis of Fig. 6 should be carried out using in addition the noise map of Fig. 8. Figures 9 and 10 shows in greater detail the absorption maps we obtain for the Ophiuchus and Lupus complexes, and allow us appreciate better the details that we can obtain by applying the NICER method to the quality of 2MASS data.

3. Statistical analysis

3.1. Reddening law

The large number of stars in the field allowed us to accurately check the reddening law used throughout this paper. To the purpose, we partitioned all stars into different bins corresponding to the individual original $\hat{A}_K^{(n)}$ measurements (we used a bin size of 0.02 mag). Then, we evaluated the average NIR colors in each group of stars in the same bin and the corresponding statistical uncertainties (estimated from on the photometry errors of the 2MASS catalog). The results obtained are shown in Fig. 11 together with the normal infrared reddening law in the 2MASS photometric system (Indebetouw et al. 2005). This plot shows that there are no significant deviations from the normal reddening law over the whole range of extinctions investigated here.

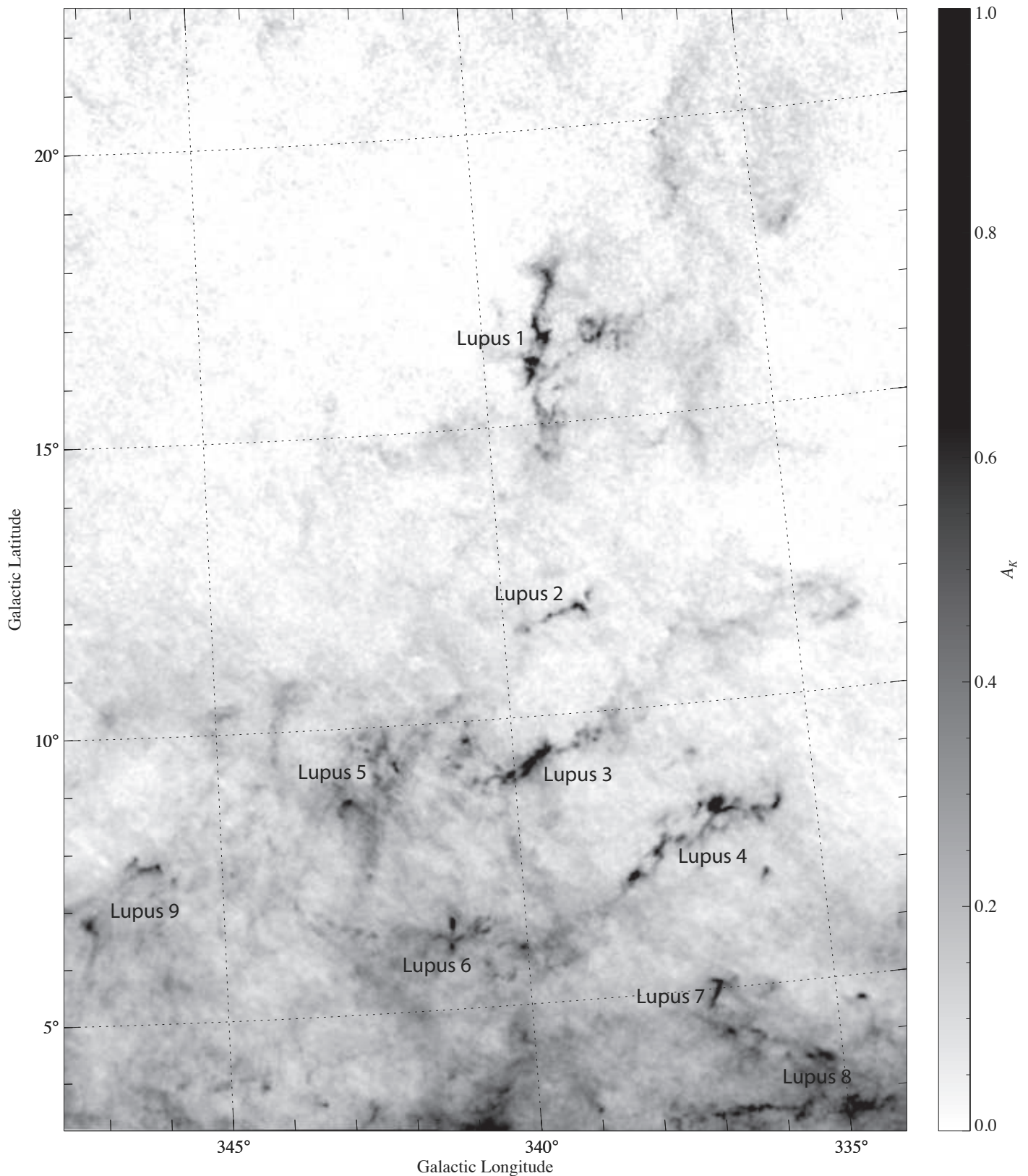


Fig. 10. A zoom of Fig. 6 showing the of Lupus cloud complex (in particular, all clouds from Lupus 1 to Lupus 9).

3.2. Foreground star contamination

If a fraction f of observed stars is foreground to a dark cloud, the measured column density is underestimated by

a factor $(1-f)$. This effect is normally negligible on the outskirts of nearby molecular clouds, where the fraction f of foreground stars is typically of the order $\sim 1\%$, but unfortunately can have significant effects on very dense regions,

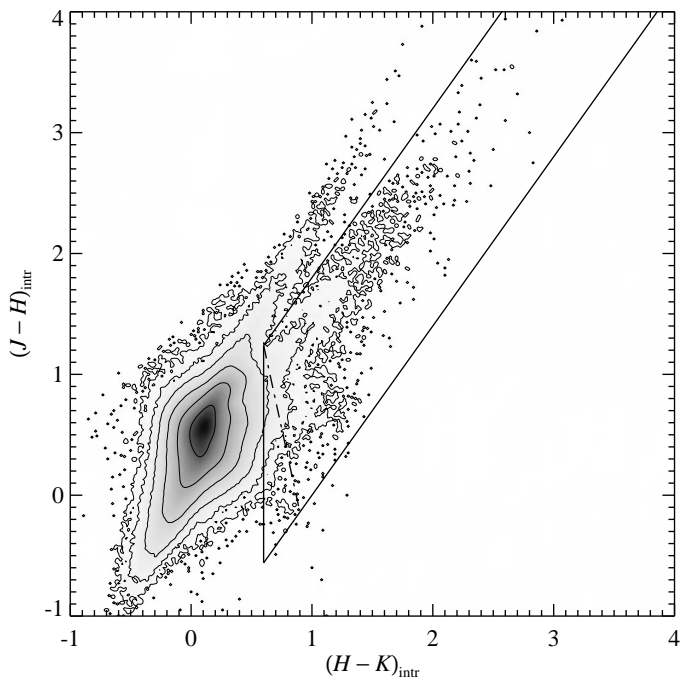


Fig. 4. The extinction-corrected color-color diagram. The stripes show both subsets B_1 and $B_2 \subset B_1$ [cf. Eqs. (7) and (8)].

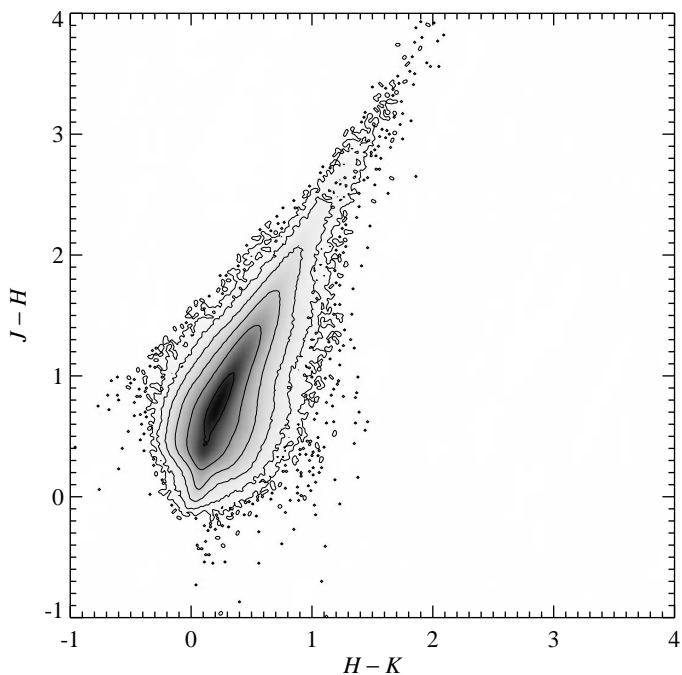


Fig. 5. The color-color diagram for the selected stars in the field, after the removal of the set B_2 of Eq. (8). A comparison with Fig. 1 shows that we were able to virtually remove all significant contamination from spurious reddening.

where because of a selection effect f increases significantly. In addition, many dense cores host young stellar objects: these stars, if moderately embedded, show only a fraction of the true, total column density of the cloud. As a result, the extinction in the direction of dense regions can be severely underestimated. For example, the core of ρ Ophiuchi shows an apparent “hole” in absorption (see Fig. 12), but a com-

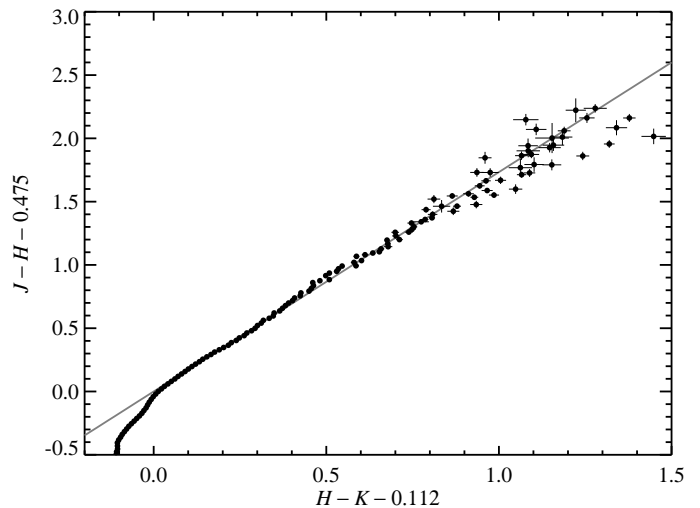


Fig. 11. The reddening law as measured on the analyzed region. The plot shows the color excess on $J - K$ as a function of the color excess on $H - K$ (the constant 0.112 and 0.475 represent, respectively, the average of $H - K$ and of $J - H$ colors in magnitudes for the control field). Error bars are uncertainties evaluated from the photometric errors of the 2MASS catalog. The solid line shows the normal infrared reddening law (Indebetouw *et al.* 2005).

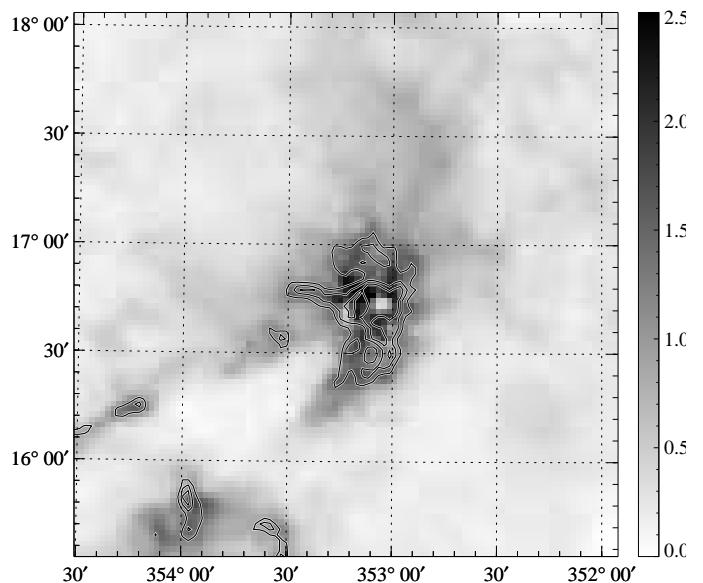


Fig. 12. A zoom of the extinction map near ρ Ophiuchi, with overprinted the star density contours. Note the white “hole” close to the center of this core, which is due to the combined effect of very high extinction values and the presence of embedded stars in this star forming core.

parison with the local density of stars shows that the hole is the result of young stars moderately embedded on this active star forming region (this core host ~ 200 young stellar objects) and of foreground star contamination (see also

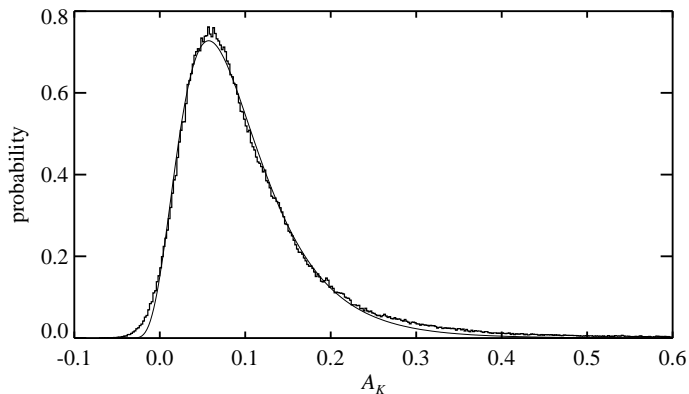


Fig. 13. The probability distribution of star pixel extinctions for the Ophiuchus map shown in Fig. 9; the gray, smooth curve represents the best-fit with a log-normal distribution.

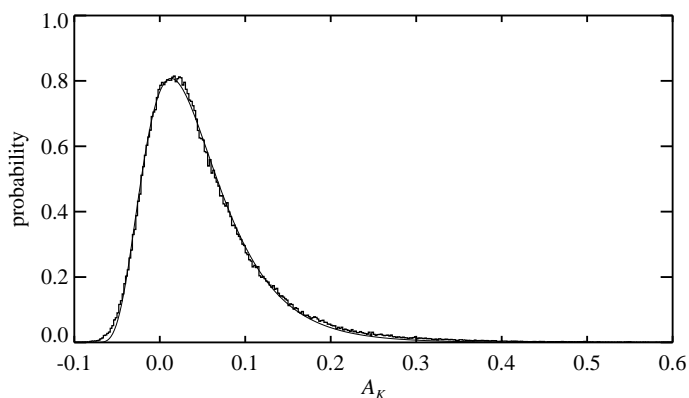


Fig. 14. The probability distribution of star pixel extinctions for the subset $b > 6.5^\circ$ of the Lupus region of Fig. 10; the gray, smooth curve represents the best-fit with a log-normal distribution.

Barsony *et al.* (1997) for a discussion on the effects of foreground stars in the ρ Ophiuchi core).

In order to evaluate quantitatively the fraction f of foreground stars, we selected high-extinction regions characterized by $A_K > 1$ mag. We then checked all stars in these regions that show “anomalous” extinction, i.e. stars whose column densities differ by more than $3\text{-}\sigma$ with respect to the field. A total of 1268 stars met this criteria, but only 784 of them show measured column densities compatible with no extinction. Hence, since the total area of regions with $A_K > 1$ mag is about 1.4 deg^2 , we estimate that on average on the field only a fraction $\sim 2\%$ of stars is foreground. As a result, we can safely ignore the effect of foreground stars except on the higher extinction regions which, however, are not the focus of this paper.

3.3. Column density probability distribution

Theoretical studies (e.g. Vázquez-Semadeni 1994; Padoan *et al.* 1997b; Passot & Vázquez-Semadeni 1998; Scalo *et al.* 1998) have shown that the probability distribution for the *volume density* in molecular clouds is log-normal for *isothermal* flows (i.e., when the polytropic index $\gamma \equiv d \ln P / d \ln \rho = 1$), while it tends to develop a power-law

tail at high (respectively, low) densities for $\gamma < 1$ ($\gamma > 1$). In reality, observations can only probe the probability distribution for the *column density*, i.e. the volume density integrated along the line of sight. As discussed by Vázquez-Semadeni & García (2001), this quantity can behave differently depending on the ratio η of the column density to a suitable defined “decorrelation length.” In particular, if η is large, so that there are many independent “events” along the line of sight, the probability distribution for the column density is expected to be normal, a result in agreement with the central limit theorem (see, e.g., Eadie *et al.* 1971); if, instead, η is small, the probability distribution for the column density is expected to be similar to the one for the volume density, i.e. log-normal in the isothermal case. In practice, numerical simulations show that the convergence to the normal distribution is extremely slow and that transition between the two cases, in typical cases, is for $\eta \simeq 10^4$ (Vázquez-Semadeni & García 2001).

Figures 13 and 14 report the probability distributions of column densities observed in the Ophiuchus and Lupus fields, i.e. the relative probability of column density measurements for each pixel of Figs. 9 and 10. We tried to fit the column density histograms with log-normal distributions of the form

$$h(A_K) = \frac{a}{A_K - A_0} \exp \left[-\frac{(\ln(A_K - A_0) - \ln A_1)^2}{2(\ln \sigma)^2} \right]. \quad (12)$$

For the Ophiuchus complex we obtained a satisfactory fit on the whole region; for Lupus, the fit is extremely good, especially when excluding the low-galactic latitude regions ($b < 6.5^\circ$), which are likely to be contaminated by different cloud complexes. Note, by comparison, that as described in Paper I, for the Pipe nebula a good fit to the column density distribution requires four normal distribution. This result might indicate that the Pipe nebula is the result of the superposition of different components, each of which is likely to be extended on the line of sight (so that the central limit theorem can be applied to the total measured column density).

3.4. Small-scale inhomogeneities

It has been long recognized (Lada *et al.* 1994) that the local dispersion of extinction measurements increases with the column density: in other words, for a fixed (small) patch of the sky, the scatter of the individual star estimates of A_K increases as the average of A_K increases. The scatter in the A_K estimates is typically associated with the intrinsic scatter in the NIR star colors and to the effect of small-scale inhomogeneities in the cloud projected density. These inhomogeneities are important for a number of factors:

	Center A_0	Scale A_1	Dispersion σ	Peak a
Ophiuchus	-0.081	0.151	0.681	946
Lupus ($b > 6.5^\circ$)	-0.135	0.153	1.506	651

Table 1. The best-fit parameters of the four Gaussian functions used to fit the column density probability distribution shown in Figs. 13 and 14 (see Eq. (12) for the meaning of the various quantities).

- In the simplest interpretation, they indicate differential extinction or strong gradients in the column density (with typical scales smaller than the resolution of the extinction map).
- If present at different scales, they can be interpreted as the effects of turbulent motions (see, e.g. Miesch & Bally 1994; Padoan *et al.* 1997a).
- In presence of significant inhomogeneities at scales smaller than the resolution of the extinction map, NICER (as well as other color-excess methods) is expected to be biased toward low extinction. This happens because the background stars will no longer be randomly distributed in the patch of the sky used to estimate the local extinction value, but will be preferentially detected in low-extinction regions (see Lombardi 2005 for a more detailed discussion on this point).

In order to better quantify the effect of inhomogeneities on small scales, consider the quantity (cf. Paper II)

$$\hat{\sigma}_{\hat{A}_K}^2(\boldsymbol{\theta}) = \frac{\sum_{n=1}^N W^{(n)} [\hat{A}_K^{(n)} - \hat{A}_K(\boldsymbol{\theta})]^2}{\sum_{n=1}^N W^{(n)}}. \quad (13)$$

Note that $\hat{\sigma}_{\hat{A}_K}^2$ is defined in a different way with respect to $\sigma_{\hat{A}_K}^2$ of Eq. (11). Let us now fix a given direction in the sky $\boldsymbol{\theta}$, and let us consider the process of measuring the column density $\hat{A}_K(\boldsymbol{\theta})$ there. This quantity is evaluated using Eq. (9), i.e. $\hat{A}_K(\boldsymbol{\theta})$ is a weighted mean of the estimated column densities $\{\hat{A}_K^{(n)}\}$ of the stars observed close to the direction $\boldsymbol{\theta}$. The estimated star column density for the n -th star, in turn, can be written as

$$\hat{A}_K^{(n)} = \tilde{A}_K + \Delta^{(n)} + \epsilon^{(n)}. \quad (14)$$

In this equation we split the three contributions to the measured column density: \tilde{A}_K , the ‘‘average’’ extinction in the patch of the sky considered (see below); $\Delta^{(n)} \equiv A_K(\boldsymbol{\theta}^{(n)}) - \tilde{A}_K$, the local difference from the average extinction, which includes both random inhomogeneities (e.g., due to turbulence) and unresolved structures (e.g., due to steep gradients in the extinction); and $\epsilon^{(n)}$, the photometric error on the measured extinction of the n -th star.

Because of the presence of the photometric error $\epsilon^{(n)}$ in Eq. (14), we cannot use directly the estimator $\hat{\sigma}_{\hat{A}_K}^2$ of Eq. (13) as a measure of small-scale inhomogeneities, and a more detailed analysis is needed. In the following we will consider *ensemble averages* with respect to the photometric errors $\epsilon^{(n)}$; in other words, we will evaluate the mean values and variances of some relevant quantities by taking $\epsilon^{(n)}$ as independent random variables with the properties

$$\langle \epsilon^{(n)} \rangle = 0, \quad \langle (\epsilon^{(n)})^2 \rangle = \text{Var}(\hat{A}_K^{(n)}) \equiv V^{(n)}, \quad (15)$$

where the last equality is a mere definition. In the decomposition of Eq. (14) we can freely choose the value of the ‘‘average’’ extinction \tilde{A}_K (a change of \tilde{A}_K can be counterbalanced by a change of all $\Delta^{(n)}$); we now fix this quantity to

$$\tilde{A}_K \equiv \frac{\sum_{n=1}^N W^{(n)} A_K(\boldsymbol{\theta}^{(n)})}{\sum_{n=1}^N W^{(n)}}. \quad (16)$$

This is a convenient and natural choice since in this case we have

$$\frac{\sum_{n=1}^N W^{(n)} \Delta^{(n)}}{\sum_{n=1}^N W^{(n)}} = 0, \quad (17)$$

and $\langle \hat{A}_K(\boldsymbol{\theta}) \rangle = \tilde{A}_K$. Note also that in this case we have

$$\hat{A}_K(\boldsymbol{\theta}) - \tilde{A}_K = \frac{\sum_{n=1}^N W^{(n)} \epsilon^{(n)}}{\sum_{n=1}^N W^{(n)}} \equiv \epsilon(\boldsymbol{\theta}). \quad (18)$$

The quantity $\epsilon(\boldsymbol{\theta})$ can be interpreted as the ‘‘error’’ on the extinction map:

$$\langle \epsilon(\boldsymbol{\theta}) \rangle = 0, \quad (19)$$

$$\langle [\epsilon(\boldsymbol{\theta})]^2 \rangle = \frac{\sum_{n=1}^N (W^{(n)})^2 V^{(n)}}{(\sum_{n=1}^N W^{(n)})^2} \equiv \sigma_{\hat{A}_K}^2(\boldsymbol{\theta}), \quad (20)$$

where in the last step we used the definition (11).

We can now finally consider the ensemble average of the quantity of Eq. (13):

$$\langle \hat{\sigma}_{\hat{A}_K}^2 \rangle = \frac{\sum_{n=1}^N W^{(n)} \langle [\Delta^{(n)} + \epsilon^{(n)} - \epsilon(\boldsymbol{\theta})]^2 \rangle}{\sum_{n=1}^N W^{(n)}}. \quad (21)$$

Using the relation

$$\langle \epsilon^{(n)} \epsilon(\boldsymbol{\theta}) \rangle = \left\langle \epsilon^{(n)} \frac{\sum_m W^{(m)} \epsilon^{(m)}}{\sum_m W^{(m)}} \right\rangle = \frac{W^{(n)} V^{(n)}}{\sum_m W^{(m)}}, \quad (22)$$

we can expand Eq. (21) into

$$\begin{aligned} \langle \hat{\sigma}_{\hat{A}_K}^2 \rangle &= \frac{\sum_n W^{(n)} (\Delta^{(n)})^2}{\sum_n W^{(n)}} + \frac{\sum_n W^{(n)} V^{(n)}}{\sum_n W^{(n)}} + \sigma_{\hat{A}_K}^2(\boldsymbol{\theta}) \\ &\quad - 2 \frac{\sum_n (W^{(n)})^2 V^{(n)}}{(\sum_n W^{(n)})^2} \\ &= \frac{\sum_n W^{(n)} (\Delta^{(n)})^2}{\sum_n W^{(n)}} + \frac{\sum_n W^{(n)} V^{(n)}}{\sum_n W^{(n)}} - \sigma_{\hat{A}_K}^2(\boldsymbol{\theta}). \end{aligned} \quad (23)$$

The first term in the r.h.s. of this equation represents a measure of small scale inhomogeneities. Since all other quantities appearing in Eq. (23) can be evaluated from the data, it makes sense to define the map

$$\begin{aligned} \Delta^2(\boldsymbol{\theta}) &\equiv \hat{\sigma}_{\hat{A}_K}^2(\boldsymbol{\theta}) + \sigma_{\hat{A}_K}^2(\boldsymbol{\theta}) - \frac{\sum_n W^{(n)} V^{(n)}}{\sum_n W^{(n)}} \\ &= \frac{\sum_n W^{(n)} (\Delta^{(n)})^2}{\sum_n W^{(n)}}, \end{aligned} \quad (24)$$

and to interpret it as a ‘‘variance’’ of small scale inhomogeneities. Note finally that if the weights $\{W^{(n)}\}$ are chosen according to Eq. (10), then in the numerator of the last term of this equation we can use $W^{(n)} V^{(n)} = W(\boldsymbol{\theta} - \boldsymbol{\theta}^{(n)})$.

We evaluated the Δ^2 map for the whole field in order to identify regions with large small-scale inhomogeneities. The outcome of this analysis (see Figs. 15 and 16) support some results recently obtained for the Pipe nebula

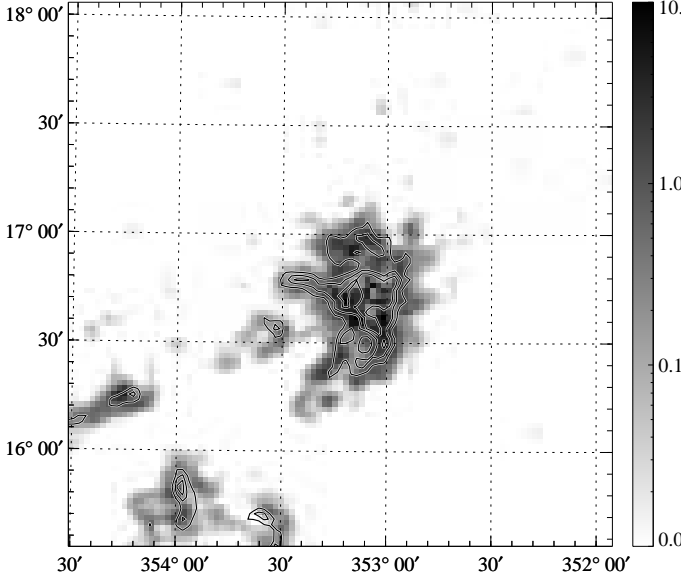


Fig. 15. The Δ^2 map of Eq. (24) on the same region around ρ Ophiuchi shown in Fig. 12, with overplotted star density contours. Note the significant increase observed in Δ^2 close to the central parts of this cloud.

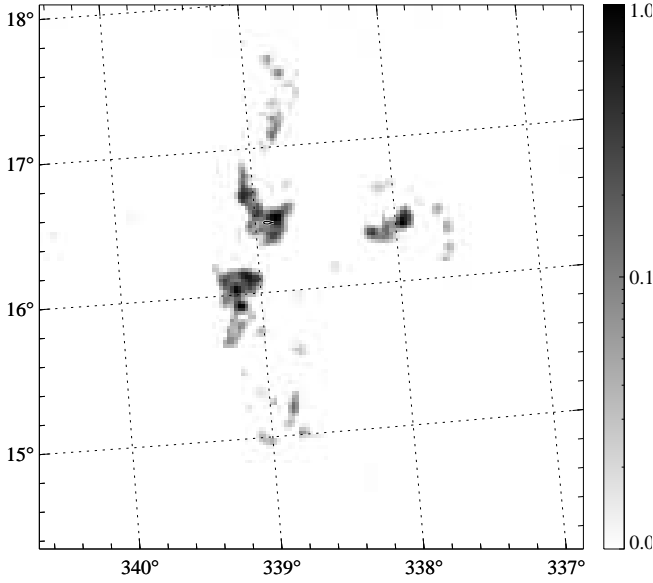


Fig. 16. The Δ^2 map of Eq. (24) on a region close to Lupus 1, in logarithmic scale, with overplotted star density contours (using the same levels as Fig. 15).

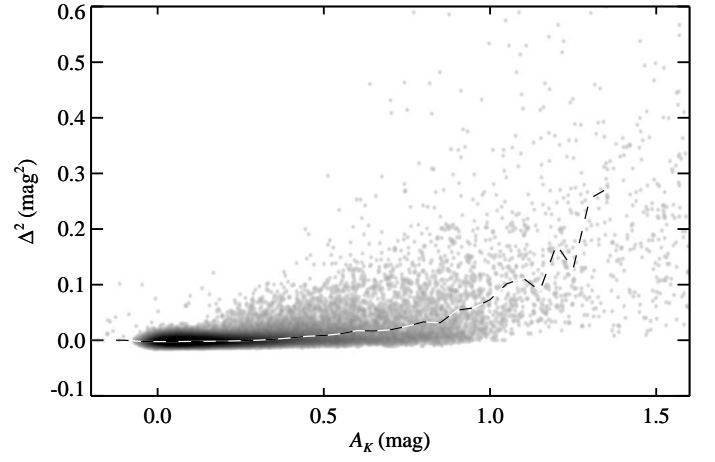


Fig. 17. The distribution of the Δ^2 map as a function of the local extinction A_K for the Ophiuchus, in logarithmic grey scale. The dashed line shows the average values of Δ^2 in bins of 0.05 mag in A_K . Note the rapid increase of Δ^2 for $A_K > 0.8$ mag. As a comparison, the average variance $\text{Var}(\hat{A}_K^{(n)})$ on the estimate of \hat{A}_K from a single star is approximately 0.033 mag^2 .

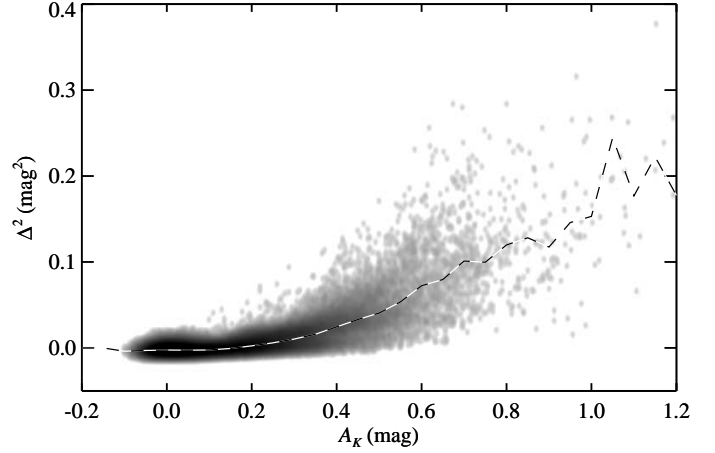


Fig. 18. Same as Fig. 17 for Lupus. Note that the effect of substructures is evident at significantly lower column densities.

(Lombardi 2008): inhomogeneities are mostly present in high column density regions, while at low extinctions (approximately below $A_K < 0.5$ mag) substructures are either on scales large enough to be detected at our resolution (3 arcmin), or are negligible. The range of values spanned by the Δ^2 map is quite impressive: it reaches $(1.5 \text{ mag})^2$ in the ρ Ophiuchi core, indicating an extraordinary amount of small-scale substructures present there. The Lupus region shows less pronounced small-scale inhomogeneities, with a maximum $\Delta^2 \simeq (0.66 \text{ mag})^2$ found in the Lupus 3 core (not shown here). The Lupus Δ^2 map at low galactic latitudes shows significant amount of substructures, possibly due to the presence of other molecular clouds (see below).

Figures 17 and 18 shows the average Δ^2 as a function of the local extinction A_K for the Ophiuchus and the Lupus clouds. As shown by these plot, substructures start to play a significant role at relatively large column densities and

are negligible at low A_K . In particular, the dashed lines in these plots, representing the average value of Δ^2 in bins of 0.05 mag in A_K , should be compared with the average variance $\text{Var}(\hat{A}_K^{(n)})$ on the estimate of \hat{A}_K from a single star, which is approximately 0.033 mag^2 . From Figs. 17 and 18 we thus see that local inhomogeneities start to be the prevalent source of errors in extinction maps for $A_K > 0.8$ mag for the Ophiuchus cloud. For the Lupus complex, apparently this happens before, but a more detailed analysis shows that this result is mostly due to the rapid increase of Δ^2 at low galactic latitudes (which, in turn, is probably due to other intervening clouds).

Diagrams such as the ones presented in Figs. 17 and 18 are invaluable to understand the small-scale properties of molecular clouds, but clearly they can only be interpreted with a detailed model. A thorough analysis of these results goes beyond the scope of this paper, and in any case is hampered by the relatively coarse resolution achievable using 2MASS data. Still these data allow us to confirm that the observed scatter in column density is due to small-scale substructure and not to other effects such as foreground star contamination. The latter, typically, show up in the A_K - Δ^2 diagram as separate trails with parabolic shape that divert from the main $\Delta^2 = 0$ locus of points (cf. Fig. 9 in Lada *et al.* 1994, where however $\hat{\sigma}_{\hat{A}_K} \sim \sqrt{\Delta^2}$ is plotted, so that the parabolic shape becomes a line). This pattern typically is well discernible, and in absence of other sources of inhomogeneities produces a clear signature that is not compatible with the results obtained in Figs. 17 and 18. In summary, the data seem to indicate a genuine presence of small-scale inhomogeneities. Although a specific, model-dependent analysis would be needed to better understand their origin, the evidence we have suggests that it is not unlikely that these substructures are associated to steep gradients (or possibly unresolved clumps) in the extinction map.

3.5. Cloud structure functions

The structure functions of the extinction map of a molecular cloud are defined as

$$S_p(\phi) \equiv \langle |A_K(\boldsymbol{\theta}) - A_K(\boldsymbol{\theta} + \boldsymbol{\phi})|^p \rangle, \quad (25)$$

where the average is carried over all positions $\boldsymbol{\theta}$ and all directions for $\boldsymbol{\phi}$ (note that for $p = 2$, the structure function $S_2(\phi)$ is the usual two-point correlation function of the extinction map A_K).

Starting from Kolmogorov (1941), one of the focuses of turbulence theory have been the *statistical* properties of the *velocity* field. In a wide range of length scales, known as “inertial range,” the effects of both external forces (which are taken to act on very large scales) and viscosity (which plays a role on very small scales) are negligible. As a result, in this range the energy of large scale flows is merely transferred to smaller scales until viscous effects become important, a process named “energy cascade.” This naturally leads to random, isotropic motions (because the imprint of the large scale flows is likely to be lost during the energy cascade), which can be studied with the help of velocity structure functions, defined similarly to $S_p(\phi)$ of Eq. (25). In his seminal paper, Kolmogorov (1941) considered the first two structure velocity functions S_2 and S_3 , and showed that both are simple power laws of the separation ϕ , with

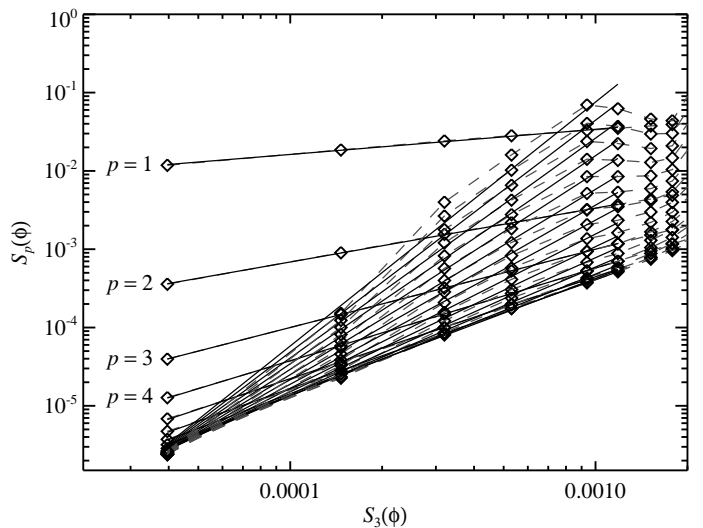


Fig. 19. The structure functions for the Ophiuchus complex. The diamonds show the measured $S_p(\phi)$ as a function of $S_3(\phi)$, with p increasing from 1 to 20; the dashed lines connect diamonds with the same p and different ϕ ; the solid lines are the best exponential fits. The first four values of p are marked at the left of the corresponding fit.

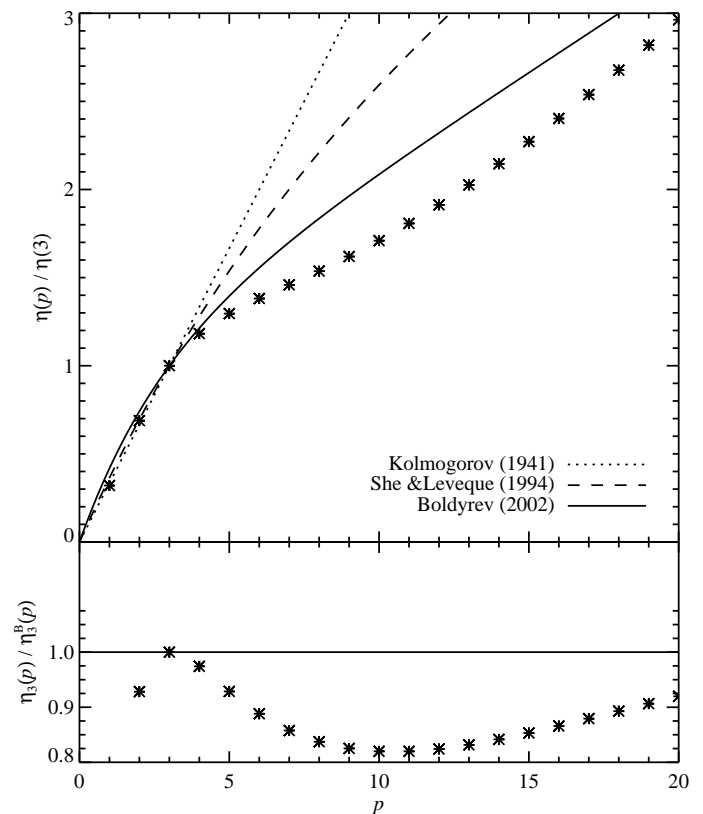


Fig. 20. The scaling index ratio $\eta(p)/\eta(3)$ as a function of the structure function order p for the Ophiuchus cloud [cf. Eq. (26)], with the predictions from three theoretical models. The bottom panel shows the ratio between the observed scaling index and the one predicted by Boldyrev (2002).

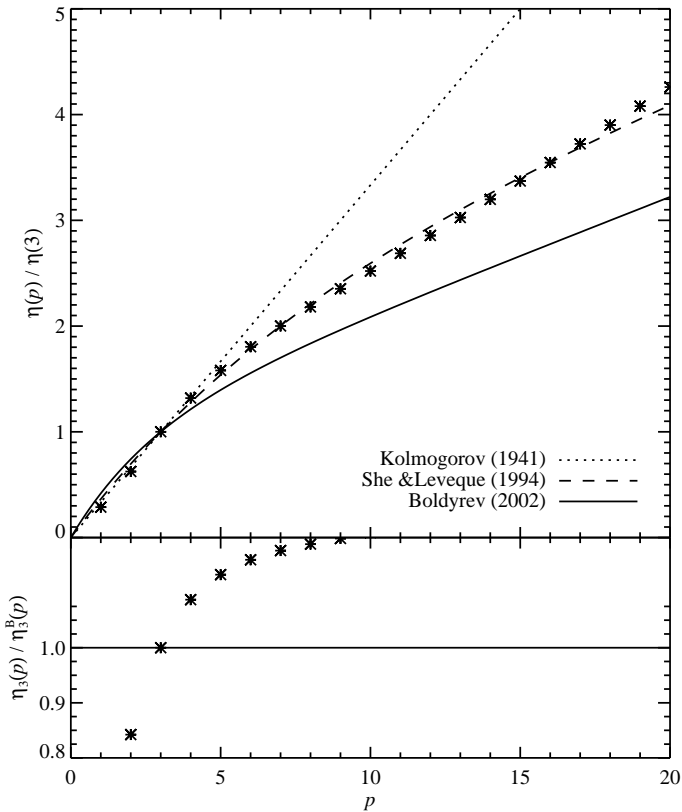


Fig. 21. Same as Fig. 20, but for the Lupus cloud. In this case the She & Leveque (1994) model seems to be able to reproduce very well the data. Note that no significant difference in the scaling index is observed when the low galactic latitude regions of the cloud are discarded in the analysis.

exponents $2/3$ and 1 . Since Kolmogorov’s theory implicitly assumes that turbulence is statistically self-similar at different scales, one can actually extend this result to any order p , and show that the structure functions of the velocity field must be simple power laws of the angular distance parameter ϕ , i.e.

$$S_p(\phi) \propto \phi^{\eta(p)}, \quad (26)$$

where $\eta(p) = p/3$ in the simplest turbulent model considered by Kolmogorov. However, experiments and numerical simulations have shown that, although Eq. (26) applies to a variety of turbulent flows at high Reynolds number, $\eta(p)$ substantially deviates from linearity at higher orders p , a phenomenon often referred to as “intermittency.” She & Leveque (1994) have proposed a model for incompressible turbulence based on intermittency, further extended by Boldyrev (2002) and tested with numerical simulations of supersonic turbulence (Boldyrev *et al.* 2002).

Although no equivalent models are available for the (projected) density of molecular clouds, we follow Padoan *et al.* (2002) and assume that the same scaling law $\eta(p)$ applies to both the velocity and density fields. We analysed thus the structure functions $S_p(\phi)$ and scaling law $\eta(p)$ for both the Ophiuchus and Lupus complexes. Figure 19 shows the observed structure functions up to $p = 20$ on the Ophiuchus complex, together with the best exponential fits (which are found to be appropriate in our case). The dependence of the exponent $\eta(p)$ of the best fit on the struc-

ture function order p is shown in Fig. 20, together with the predictions of the three turbulent models discussed above. Note that in this analysis we considered the ratio $\eta(p)/\eta(3)$, which according to Benzi *et al.* (1993) (see also Dubrulle 1994) should show a universal behaviour also at relatively small Reynolds numbers. While the Boldyrev model seems to fit reasonably well the data for the Taurus molecular cloud (Padoan *et al.* 2002), the fit seems to be very poor for the Ophiuchus and Lupus complexes (Figs. 20 and 21).

Despite the fact that the interpretation of these results can be complicated by many factors, the data analysed here seems to indicate that the Ophiuchus and Lupus clouds have two intrinsically different structure functions. In addition, Figs. 20 and 21 show that one of the currently favoured turbulent models, the Boldyrev (2002) model, can not describe accurately the large-scale structure of these molecular clouds. Interestingly, for the Lupus complex a good description of the scaling index ratio $\eta(p)/\eta(3)$ is instead given by the She & Leveque (1994) model, with relatively small deviations over the whole range of p values investigated here. Note that, by construction, the structure function index $\eta(p)$ is left unchanged by a simple linear (affine) transformation $A_K(\theta) \mapsto \alpha A_K(\theta) + \beta$ of the extinction map, and thus is insensitive to errors on the zero-point of the extinction (control field) and on the reddening law. Similarly, the structure function index is independent of the distance of the cloud: in other words, if two physically identical cloud located at different distances d and d' will have structure functions that differ only by a scaling factor:

$$S'_p(\phi) = S_p(k\phi), \quad (27)$$

where $k = d/d'$, we have

$$\phi'^{\eta'(p)} \propto S'_p(\phi) = S_p(k\phi) \propto k^{\eta(p)} \phi^{\eta(p)} \propto \phi^{\eta(p)}, \quad (28)$$

or $\eta'(p) = \eta(p)$. Note, however, that if two clouds located at different distances and with the same structure function index $\eta(p)$ (or even with the same structure functions S_p) are analysed jointly in the same field, the deduced structure functions will in general exhibit a non-trivial behaviour, and will not be simply described as power laws as in Eq. (26). Since this paper focuses on two wide molecular cloud complexes, this point might potentially affect the results and partially be responsible for the poor fits displayed in Figs. 20 and 21. Hence, we decided to repeat the analysis in the core of Ophiuchus (see window marked with solid line in Fig. 9) which is most likely composed by a single cloud at a well determined distance (e.g. Lombardi *et al.* 2008), but the results obtained are completely consistent to the ones shown in Fig. 20. This, indirectly, confirms that for the purposes of the calculation of the cloud structure function, there is no significant difference in using the whole Ophiuchus complex or a smaller subset centered on its core, or equivalently that most likely the poor fit observed for this cloud with the turbulent models considered here is not due to the overlapping, distinct clouds located at different distances. Finally, we stress that the conclusions reported here seems to be robust against cuts of the star catalogue (see Sect. 2) and to changes in the resolution of our maps.

Cloud	Total mass	Cloud mass
Ophiuchus	25 400 M_{\odot}	8 300 M_{\odot}
Lupus	36 500 M_{\odot}	18 200 M_{\odot}
Pipe	14 800 M_{\odot}	14 200 M_{\odot}
Pipe (corrected)	9 200 M_{\odot}	7 600 M_{\odot}

Table 2. The masses of the Ophiuchus, Lupus, and Pipe dark complexes. For the Pipe, the “corrected” values reported in the last line refer to the extinction map corrected for the 0.15 mag plateau. The two columns refers to the whole fields considered here, and to the regions with $A_K > 0.2$ mag only.

4. Mass estimate

The cloud mass M can be derived from the A_K extinction map using the following simple relation

$$M = d^2 \mu \beta_K \int_{\Omega} A_K(\theta) d^2\theta, \quad (29)$$

where d is the cloud distance, μ is the mean molecular weight corrected for the helium abundance, $\beta_K \simeq 1.67 \times 10^{22} \text{ cm}^{-2} \text{ mag}^{-1}$ is the ratio $[N(\text{HI}) + N(\text{H}_2)]/A_K$ (Savage & Mathis 1979; see also Lilley 1955; Bohlin *et al.* 1978), and the integral is evaluated over the whole field Ω . Assuming a standard cloud composition (63% hydrogen, 36% helium, and 1% dust), we find $\mu = 1.37$ and total masses $M = (25\,400 \pm 2\,500) M_{\odot}$ for Ophiuchus, and $M = (36\,500 \pm 3\,600) M_{\odot}$ for Lupus (cf. Table 2). The error in both cases is mainly due to the uncertainty on the distance of the cloud (for both clouds we used our new distance measurements, see Lombardi *et al.* 2008); in addition, for Lupus there is an additional uncertainty (not included in our error budget) due to the possible projection of other clouds on the line of sight. We also considered the total mass of the Pipe nebula from our data. As shown by Fig. 6, the Pipe nebula is located in an area of fairly large extinction, and as a result it is reasonable to subtract from the extinction map of the Pipe a constant value, representing the “plateau” where the Pipe nebula is located. Clearly, an exact, physically meaningful definition of the value cannot be provided from the available data, because there is no simple way to disentangle the effects of different cloud structures located at different distances from near-infrared extinction measurements alone. Hence, we decided here to derive the value of the “plateau” extinction from the same area used as a control field in Paper II. This choice is reasonable, because it selects the lowest extinction values on the area around the Pipe nebula, and in addition produces results that are comparable to the ones provided in Paper II. Finally, additionally we considered only regions above 0.2 mag of K -band extinction: this choice allows us to concentrate on the real structures present in the cloud complexes and to avoid the diffuse, low-density material surrounding them. The results obtained for the various combinations discussed here are reported in Table 2.

Figure 22 shows the relationship between the integrated mass distribution and the extinction in A_K ; for the Pipe nebula, we used the “corrected” extinction with the plateau subtracted. Note that regions with extinction larger than $A_K > 1$ mag account for less than 1% of the total mass in the whole field. Hence, we do not expect any significant underestimation in the cloud mass due to unresolved dense cores.

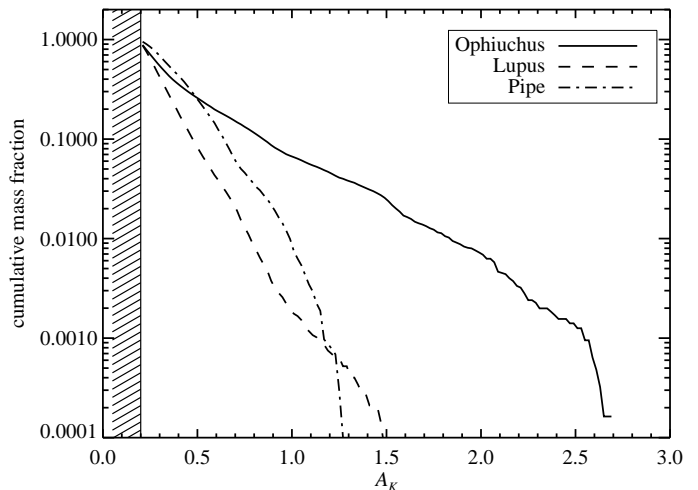


Fig. 22. The cumulative mass enclosed in isoextinction contours for the Ophiuchus, Lupus, and Pipe molecular clouds. All plots have been obtained from the extinction map shown in Fig. 6, and have thus the same resolution limit. Note that the difference between the Pipe nebula cumulative mass function shown here and the one reported in Fig. 27 of Paper II is essentially due to the different resolution of the two extinction maps.

More significantly Fig. 22 also shows a clear difference between the relative frequencies of extinction characterizing the Ophiuchus, Lupus and Pipe clouds. Ophiuchus has a considerably higher fraction of dust at high extinction ($A_K > 1.0$ mag) than either Lupus or the Pipe. This reinforces the result of Sect. 3.5 that shows a significant difference in the structural properties of the Ophiuchus and Lupus clouds at high order p of the structure function. The scaling index curve for Ophiuchus (Fig. 20) is significantly flatter than the corresponding curve for the Lupus cloud (Fig. 21) and the predictions of turbulence theory. Inspection of Eq. (25) indicates that this difference is a direct result of the Ophiuchus cloud having a larger fraction of its material at high extinction compared both to that in the Lupus cloud or that predicted by standard turbulence theory.

It is interesting to note in this context that it has been known for some time (e.g. Lada 1992) that star formation occurs almost exclusively in dense ($n(\text{H}_2) > 10^4 \text{ cm}^{-3}$), high extinction ($A_V > 10$ mag) gas. Thus, it is not surprising that the Ophiuchus cloud is a very active star formation complex, the site of a relatively rich embedded cluster. In contrast, Lupus is characterized by more modest levels of star formation (e.g. Teixeira *et al.* 2005) and the Pipe cloud is noted for its nearly complete absence of star forming activity (e.g. Alves *et al.* 2008). The closer correspondence of the Lupus structure function to the predictions of turbulence theory (Fig. 21) compared to that of Ophiuchus (Fig. 20) may indicate that standard turbulence inhibits the large scale production of dense gas and suppresses active star and cluster formation.

5. Conclusions

The main results of this paper can be summarized as follows:

- We used approximately 42 million stars from the 2MASS point source catalog to construct a 1 672 square degrees NICER extinction map of the Ophiuchus and Lupus dark nebulae. The map has a resolution of 3 arcmin and an average 2σ detection level of 0.5 visual magnitudes.
- We considered in detail the effect of sub-pixel inhomogeneities, and derived an estimator useful to quantify them. We also showed that inhomogeneities play a significant role only in the densest cores with $A_K > 6$ –8 mag.
- We derived the structure functions of both dark clouds and compared them with several theoretical models. We could not find any reasonable fit of the Ophiuchus data with models, while the Lupus scaling index ratio is well described in terms of the She & Leveque (1994) turbulent model.

Acknowledgements. We thank the anonymous referee for many useful comments and suggestions. This research has made use of the 2MASS archive, provided by NASA/IPAC Infrared Science Archive, which is operated by the Jet Propulsion Laboratory, California Institute of Technology, under contract with the National Aeronautics and Space Administration. CJL acknowledges support from NASA ORIGINS Grant NAG 5-13041.

References

Alves, J., Lombardi, M., & Lada, C. 2008, in Handbook of low mass star formation regions, ed. B. Reipurth, ASP Conference Series
 Barsony, M., Kenyon, S. J., Lada, E. A., & Teuben, P. J. 1997, ApJS, 112, 109
 Benzi, R., Ciliberto, S., Tripicciono, R., et al. 1993, Phys. Rev. E, 48, 29
 Bertout, C., Robichon, N., & Arenou, F. 1999, A&A, 352, 574
 Bohlin, R. C., Savage, B. D., & Drake, J. F. 1978, ApJ, 224, 132
 Boldyrev, S. 2002, ApJ, 569, 841
 Boldyrev, S., Nordlund, Å., & Padoan, P. 2002, ApJ, 573, 678
 Bontemps, S., André, P., Kaas, A. A., et al. 2001, A&A, 372, 173
 Cameron, F., Rieke, G. H., Burrows, A., & Rieke, M. J. 1993, ApJ, 416, 185
 de Geus, E. J. 1992, A&A, 262, 258
 Dubrulle, B. 1994, Physical Review Letters, 73, 959
 Eadie, W., Drijard, D., James, F., Roos, M., & Sadoulet, B. 1971, Statistical Methods in Experimental Physics (Amsterdam New-York Oxford: North-Holland Publishing Company)
 Greene, T. P. & Young, E. T. 1992, ApJ, 395, 516
 Hughes, J., Hartigan, P., Krautter, J., & Kelemen, J. 1994, AJ, 108, 1071
 Indebetouw, R., Mathis, J. S., Babler, B. L., et al. 2005, ApJ, 619, 931
 Johnstone, D., Wilson, C. D., Moriarty-Schieven, G., et al. 2000, ApJ, 545, 327
 Kleinmann, S. G., Lysaght, M. G., Pughe, W. L., et al. 1994, Experimental Astronomy, 3, 65
 Knude, J. & Hog, E. 1998, A&A, 338, 897
 Knude, J. & Nielsen, A. S. 2001, A&A, 373, 714
 Kolmogorov, A. N. 1941, Dokl. Akad. Nauk SSSR, 30, 301
 Krautter, J. 1991, in European Southern Observatory Scientific Report, Vol. 11, Low Mass Star Formation in Southern Molecular Clouds., ed. B. Reipurth, J. Brand, J. G. A. Wouterloot, G. H. Herbig, B. Pettersson, R. D. Schwartz, L.-A. Nyman, J. Krautter, J. A. Graham, B. A. Wilking, & C. Eiroa, 127
 Lada, C. J., Lada, E. A., Clemens, D. P., & Bally, J. 1994, ApJ, 429, 694
 Lada, E. A. 1992, ApJ, 393, L25
 Lilley, A. E. 1955, ApJ, 121, 559
 Lombardi, M. 2002, A&A, 395, 733
 Lombardi, M. 2005, A&A, 438, 169
 Lombardi, M. 2008, submitted to A&A
 Lombardi, M. & Alves, J. 2001, A&A, 377, 1023
 Lombardi, M., Alves, J., & Lada, C. J. 2006, A&A, 454, 781
 Lombardi, M., Lada, C. J., & Alves, J. 2008, A&A, 480, 785

Miesch, M. S. & Bally, J. 1994, ApJ, 429, 645
 Motte, F., Andre, P., & Neri, R. 1998, A&A, 336, 150
 Murphy, D. C., Cohen, R., & May, J. 1986, A&A, 167, 234
 Nakajima, Y., Tamura, M., Oasa, Y., & Nakajima, T. 2000, AJ, 119, 873
 Padoan, P., Cambrésy, L., & Langer, W. 2002, ApJ, 580, L57
 Padoan, P., Jones, B. J. T., & Nordlund, A. P. 1997a, ApJ, 474, 730
 Padoan, P., Nordlund, A., & Jones, B. J. T. 1997b, MNRAS, 288, 145
 Passot, T. & Vázquez-Semadeni, E. 1998, Phys. Rev. E, 58, 4501
 Savage, B. D. & Mathis, J. S. 1979, ARA&A, 17, 73
 Scalo, J., Vázquez-Semadeni, E., Chappell, D., & Passot, T. 1998, ApJ, 504, 835
 Schwartz, R. D. 1977, ApJS, 35, 161
 She, Z.-S. & Leveque, E. 1994, Physical Review Letters, 72, 336
 Stanke, T., Smith, M. D., Gredel, R., & Khanzadyan, T. 2006, A&A, 447, 609
 Tachihara, K., Abe, R., Onishi, T., Mizuno, A., & Fukui, Y. 2000, PASJ, 52, 1147
 Tachihara, K., Toyoda, S., Onishi, T., et al. 2001, PASJ, 53, 1081
 Teixeira, P. S., Lada, C. J., & Alves, J. F. 2005, ApJ, 629, 276
 Vázquez-Semadeni, E. 1994, ApJ, 423, 681
 Vázquez-Semadeni, E. & García, N. 2001, ApJ, 557, 727
 Wichmann, R., Bastian, U., Krautter, J., Jankovics, I., & Rucinski, S. M. 1998, MNRAS, 301, L39+
 Wilking, B. A. & Lada, C. J. 1983, ApJ, 274, 698